Editors' Suggestion | Featured in Physics

Tuning the Random Walk of Active Colloids: From Individual Run-and-Tumble to Dynamic Clustering

Hamid Karani,[1] Gerardo E. Pradillo,[2] and Petia M. Vlahovska[1,2]
[1]Engineering Sciences and Applied Mathematics, Northwestern University, Evanston, Illinois 60208, USA
[2]Mechanical Engineering, Northwestern University, Evanston, Illinois 60208, USA

(Received 1 August 2019; published 14 November 2019)

Active particles such as swimming bacteria or self-propelled colloids spontaneously self-organize into large-scale dynamic structures. The emergence of these collective states from the motility pattern of the individual particles, typically a random walk, is yet to be probed in a well-defined synthetic system. Here, we report the experimental realization of tunable colloidal motion that reproduces run-and-tumble and Lévy trajectories. We utilize the Quincke effect to achieve controlled sequences of repeated particle runs and random reorientations. We find that a population of these random walkers exhibit behaviors reminiscent of bacterial suspensions such as dynamic clusters and mesoscale turbulentlike flows.

DOI: 10.1103/PhysRevLett.123.208002

Microswimmers such as motile bacteria and active colloids individually perform random walks but collectively move in a much more complex fashion [1–3]. *E. coli*, for example, run-and-tumbles by executing persistent straight runs interrupted by random changes in the direction of motion and in a dense suspension generates turbulentlike flows [4–6]. Diverse biomotility strategies have inspired great interest in the engineering of artificial self-propelled particles that mimic the elaborate locomotion patterns and collective behaviors of their biological counterparts [7–11]. Most available experimental designs of artificial colloidal microswimmers perform active Brownian motion [12–21], where the reorientation in the directed motion is driven by the rotational diffusion of the swimmer. This results in slow and continuous directional changes, in contrast to the sudden turning events characteristic of the run-and-tumble bacteria. Efforts to emulate the kinetics of the bacterial run-and-tumble motions [22,23] have been unable to achieve truly random reorientation events. Only recently, reorientation disentangled from rotational diffusion has been accomplished by using viscoelastic fluid as a suspending medium [24], but control over the walk characteristics was limited.

Here we report the experimental realization of a motile colloid inspired by the Quincke roller [25–27] that performs finely tunable, diverse random walks such as run-and-tumble or Lévy walks. This Quincke random walker enables the experimental study of active fluids emulating bacterial suspensions under well-defined and controllable conditions, e.g., particle density, speed (i.e., activity), and locomotion type. A population of the Quincke random walkers display collective dynamics reminiscent of bacterial suspensions such as self-organization into swarms and various dynamic clusters.

The colloid "run" is powered by Quincke rotation, i.e., the spontaneous spinning of a particle polarized in a uniform direct current (dc) electric field [28] [see Fig. 1(a) and Supplemental Material [29] for a detailed description of the phenomenon]. If the sphere is on a surface, it rolls steadily following a straight trajectory. The Quincke rollers have stirred a lot of interest since they were discovered to undergo collective directed motion [25,26,39,40]. Our strategy to introduce a "tumble" in the colloid trajectory exploits a unique feature of the Quincke instability: the degeneracy of the rotation axis in the plane perpendicular to the applied electric field (and parallel to the rolling surface). A sequence of on-off-on electric field causes the sphere to roll-stop-turn; the turn is due to the Quincke instability picking a new axis of rotation. One caveat though is that the charging and discharging of the particle occurs by conduction and require finite time. The induced dipole $\mathbf{P}$ evolves as [41]

$$\frac{\partial \mathbf{P}}{\partial t} = \mathbf{\Omega} \times \mathbf{P} - \tau_{\mathrm{MW}}^{-1}(\mathbf{P} - \chi_e \mathbf{E}), \tag{1}$$

where $\mathbf{\Omega}$ is the rotation rate, and χ_e is the electric susceptibility of the particle. The characteristic timescale for polarization relaxation is the Maxwell-Wagner time $\tau_{\mathrm{MW}} = (\varepsilon_p + 2\varepsilon_s)/(\sigma_p + 2\sigma_s)$, which depends solely on the fluid and particle conductivities and permittivities σ and ε. Random reorientation after each run is only ensured if the sphere is completely discharged before the field is turned on. Incomplete depolarization acts as a memory and correlates subsequent runs. Thus, the relaxation nature of the polarization adds another functionality to the Quincke walks: a variable degree of run correlation. Furthermore, since the Maxwell-Wagner "memory" timescale depends solely on the fluid and particle electric properties, it can be tuned by adding surfactants to the oil [27].

Experimentally, we apply external electric field by designing a sequence of electric pulses with duration τ_R

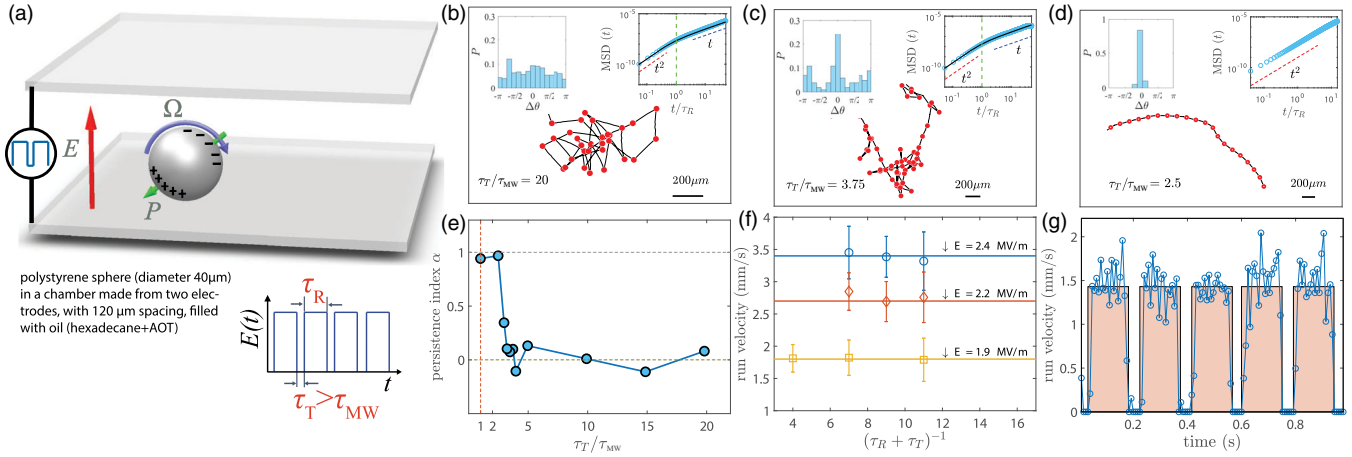

FIG. 1. (a) Quincke random walker: In a uniform direct current electric field E, free charges brought by conduction accumulate at the particle surface. For E values above the threshold for Quincke rotation, a spontaneous symmetry breaking of the charge distribution gives rise to a net torque, and the sphere rolls about a randomly chosen axis in the plane perpendicular to the applied field direction. If a square-wave electric field is applied with a period between the pulses longer than the time needed for the sphere to depolarize (Maxwell-Wagner time), the sphere executes a random walk. (b)–(d) Quincke walker trajectories at different $\tau_T/\tau_{\mathrm{MW}}$ ratios, with $\tau_R = 0.15$ s. Particle stops are marked with red circles. Insets: (Left) tumbling angle distribution, (right) log-log plot of time-averaged experimental (symbol) and theoretical (solid line) mean-squared displacement (crossover marked by the vertical dashed line at $t = \tau_R$). (e) persistence index α for different $\tau_T/\tau_{\mathrm{MW}}$ ratios. (f) Run velocity depends solely on the amplitude of the applied electric field. Symbols: Measured velocity at different amplitude and frequencies $1/(\tau_R + \tau_T)$ of the applied pulsed signal. Solid lines: Velocity measured in dc fields. (g) Particle velocity for 1 s duration of the pulsed signal $\tau_T/\tau_{\mathrm{MW}} = 20$, $\tau_R = 0.15$ s. $E = 1.66$ MV/m.

and spaced in time by τ_T to dielectric (polystyrene) micron-sized spheres (diameter 40 μm) settled onto the bottom electrode of a chamber filled with oil (hexadecane + AOT, $\tau_{\mathrm{MW}} \sim 2$ ms) [Fig. 1(a)] [27]. As predicted, various trajectories are realized depending on the degree of depolarization, i.e., $\tau_T/\tau_{\mathrm{MW}}$ [Figs. 1(b)–1(d)]. If $\tau_T \gg \tau_{\mathrm{MW}}$, particle polarization relaxes completely, and full randomization of the consecutive run directions is accomplished. As the particle trajectory and tumbling angle distribution in Fig. 1(b) show, the run and turn phases are independent, and the particle undergoes an unbiased and uncorrelated random walk. The time-averaged mean-squared displacement of the individual trajectory in Fig. 1(b) and also the ensemble average of multiple realizations (Fig. S3 in the Supplemental Material [29]) show excellent quantitative agreement with the theoretical predictions (summarized in the Supplemental Material [29]). The transition from a ballistic to diffusive motion occurs at time $t \sim \tau_R$, and the long-time behavior ($t \gg \tau_R$) follows $V^2\tau_R^2 t/(\tau_R + \tau_T)$. Typical run velocities $V \sim 1$ mm/s result in an effective diffusion coefficient on the order of a few mm^2/s, quite large for a microswimmer. As τ_T approaches τ_{MW}, the colloid motion starts to exhibit some local directional bias manifested by the emergence of a peak at a tumbling angle of zero; see Figs. 1(c) and 1(d). Eventually, the random walk vanishes completely, and the particle undergoes a persistent directed motion [Fig. 1(d)]. The trajectory is curved instead of a straight line because particle density is not uniform. The transition from the uncorrelated random walk to directed motion is illustrated in Fig. 1(e) by the persistence index $\alpha = \langle \cos(\Delta\theta) \rangle$, which quantifies the average change in the direction of motion after a run. $\Delta\theta$ is the angle between two consecutive run segments, and $\langle . \rangle$ is the average over all reorientation events. The sharp transition around $\tau_T/\tau_{\mathrm{MW}} \sim 2$ highlights the fact that complete depolarization and repolarization each occurring on a timescale $\sim\tau_{\mathrm{MW}}$ are necessary for the randomization of direction of motion. Thus, in our design for a random walker, any resting time τ_T sufficiently larger than τ_{MW} guarantees full randomization. At $\tau_T/\tau_{\mathrm{MW}} \sim 2.9$, the correlated run of the particle results in a persistence index of $\alpha = 0.345$, close to the run-and-tumble locomotion of *E. coli* [42].

The average run velocity is independent of the frequency of the electric field signal and is equal to the velocity with which the particle cruises at time-independent dc field with the same magnitude [Fig. 1(f)]. Therefore, run velocity can be controlled by the amplitude of the applied signal. Closer inspection of the particle motion shows that the particle follows the applied electric signal during the run and rest phases [Fig. 1(g) and Supplemental Material Fig. S2 [29]).

Run-and-tumble and Lévy walks.—We now proceed to construct more complex locomotion patterns. In the run-and-tumble walk, the run-times are exponentially distributed $\psi_R = 1/\bar{\tau}e^{-t/\bar{\tau}}$, where $\bar{\tau}$ is the mean value for the run times [43]. For a Lévy walk with resting periods [44], $\psi_R = \gamma t_0^{\gamma} t^{-(1+\gamma)} H(t - t_0)$, where $\bar{\tau} = t_0\gamma/(\gamma - 1)$ [43], where H is the Heaviside function, and t_0 is the lower cutoff value for the run times. The power $1 < \gamma < 2$ controls the degree of anomalous superdiffusion manifested

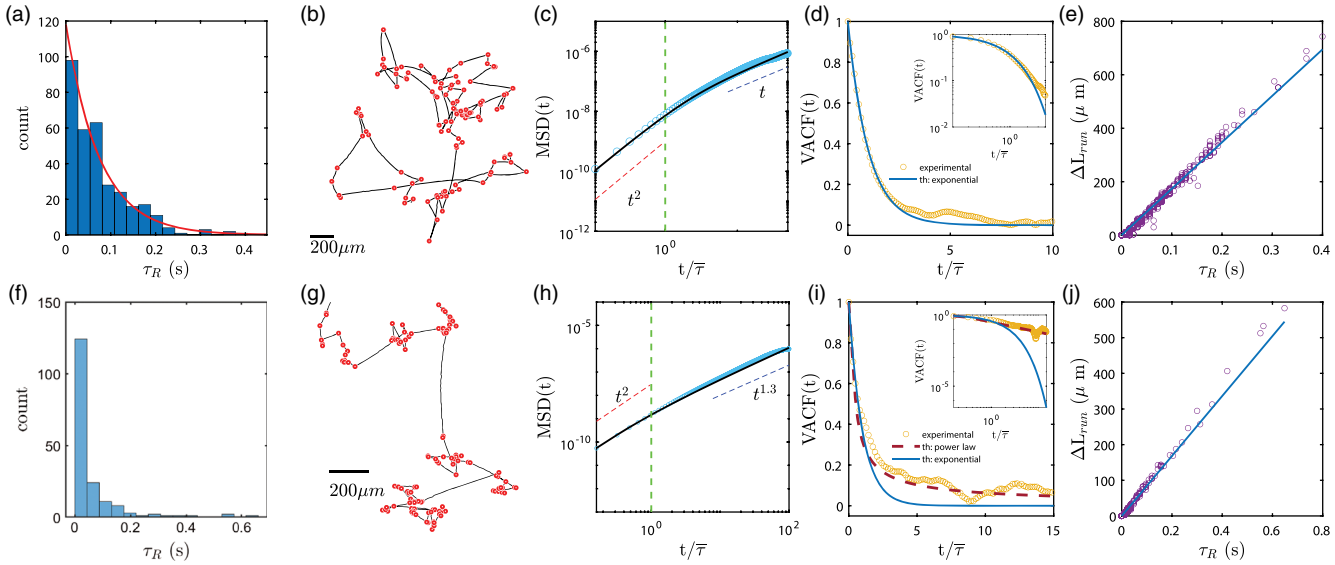

FIG. 2. Top row: Run and tumble. Bottom row: Lévy walk. (a)–(f) Distribution of run-time τ_R drawn from an exponential and power-law probability density function. (b),(g) Trajectory of the Quincke walker performing a run-and-tumble and Lévy walk. (c),(h) Time-averaged mean-squared displacement (in m^2). Symbols, experiment; solid line, theory; vertical dashed line marks $\bar{\tau}$. (d),(i) Normalized velocity autocorrelation function. Symbols, experiment; solid line, theoretical exponential decay; dashed line, theoretical power-law decay. Inset: Same in log-log scale plot. (e),(j) Run length vs the corresponding run-time τ_R. Symbols, experiment; solid line, linear fit showing a constant run velocity of $V = 1.73$ mm/s for run-and-tumble and $V = 0.84$ m/s for Lévy walk. $E = 1.83$ MV/m for run-and-tumble and $E = 1.5$ MV/m for Lévy walks. For both run-and-tumble and Lévy walk: $\bar{\tau} = 0.075$ s, $\tau_T/\tau_{\mathrm{MW}} = 20$. $\gamma = 1.7$ for Lévy walk.

at long times. In both cases, the turning time τ_T and run velocity V are constant. We randomly draw run times τ_R from ψ_R [Figs. 2(a) and 2(f)] and encode these times as pulse durations in the electric signal (sample signals are shown in Fig. S4 in the Supplemental Material [29]).

Sample trajectories of the Quincke roller performing a run-and-tumble motion and Lévy walk are shown in Figs. 2(b) and 2(g) (see also Video S1 in the Supplemental Material [29]). The measured time-averaged mean-squared displacement of an individual trajectory [Fig. 2(c)] and the ensemble average of multiple realizations (Fig. S5 in the Supplemental Material [29]) display a transition from the initial ballistic regime for times shorter than $\bar{\tau}$ to final normal diffusion with a linear scaling with time in the case of run-and-tumble. The experimental results are in excellent agreement with the theoretical prediction [43]. The mean-squared displacement for the Lévy walk [Fig. 2(h); see also Fig. S6 in the Supplemental Material [29]] exhibits superdiffusion consistent with the theoretical scaling of $t^{3-\gamma}$ [Eq. (S9) in the Supplemental Mateiral [29]]. The experimental velocity autocorrelation function VACF shown in Fig. 2(d) decays sharply in the case of run-and-tumble motion, in agreement with the theoretical predictions [Eq. (S10) in the Supplemental Material [29]]. For the Lévy walk, VACF exhibits a tail [Fig. 2(i)], as predicted theoretically [Eq. (S11) in the Supplemental Material [29]] and is poorly fitted by an exponential curve. This, plus the fact that particle's displacement follows the desired distribution, corroborates that the walker undergoes a Lévy walk. The run length [Figs. 2(e) and 2(j)] linearly depends on the corresponding run times, which confirms that the walker runs at almost constant speed.

Collective dynamics.—A population of Quincke random walkers exhibit various collective dynamics illustrated in Fig. 3 for the case of a simple walk. The collective states emerge from any initial random state, reaching steady state typically within a minute. At a given particle density, depending upon the run-time τ_R and the degree of depolarization $\tau_T/\tau_{\mathrm{MW}}$ (memory), the Quincke colloids self-organize into different dynamical phases at (statistically) steady state with distinct statistical properties, e.g., the spatial two-point correlation function S_2, velocity autocorrelation function C_{vv}, and the polar order parameter Φ_O [see Figs. 4(a)–4(c) and Supplemental Material [29] for cluster identification criteria and definitions of cluster statistics]. The classical run-only Quincke rollers [25] correspond to $\tau_T/\tau_{\mathrm{MW}} = 0$.

If the colloid run directions are correlated due to significant memory effect ($\tau_T/\tau_{\mathrm{MW}} < 2$), particles form swarms similar to those observed in the dc limit [25,26] (Video S2 in the Supplemental Material [29]). The fast decay of S_2 in Fig. 4(a) and the corresponding characteristic length scale L_{S_2} of a few particle diameter d (L_{S_2} defined as the length where S_2 crosses the horizontal line corresponding to the $r \to \infty$ limit) indicate lack of connectivity or large-scale clustering of the particles. However, swarms

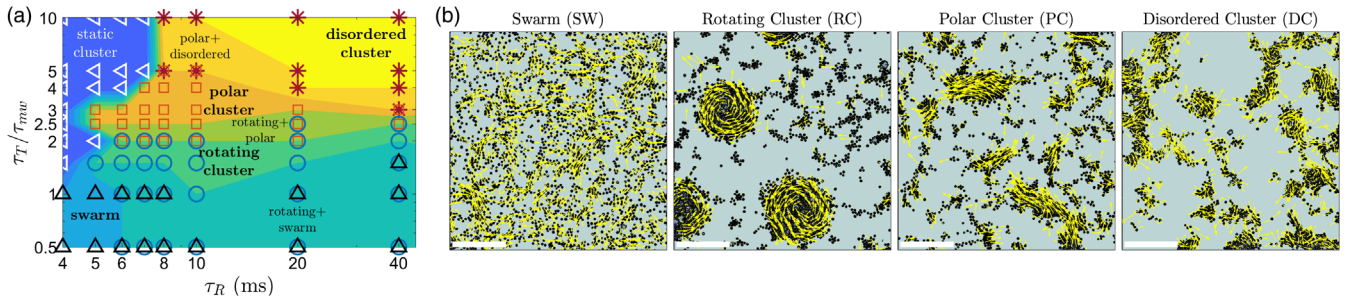

FIG. 3. (a) Collective states formed by Quincke random walkers with different run and turn times (τ_R, τ_T). Symbols indicate the experimentally observed ◁ static clusters, △ swarm (SW), ∘ rotating clusters (RC), □ polar clusters (PC), * disordered clusters (DC). (b) Snapshots of the SW ($\tau_T/\tau_{\mathrm{MW}} = 0.5$, $\tau_R = 4$ ms), RC ($\tau_T/\tau_{\mathrm{MW}} = 1.5$, $\tau_R = 5$ ms), PC ($\tau_T/\tau_{\mathrm{MW}} = 3$, $\tau_R = 8$ ms), and DC ($\tau_T/\tau_{\mathrm{MW}} = 10$, $\tau_R = 40$ ms) phases from the experiments. Scale bar is 1 mm. Velocity vectors are superimposed to the particles. Particle area fraction and pulse amplitude are constant in all experiments and are equal to $\phi \approx 0.15$ and $E = 2.08$ MV/m, respectively.

show long-range velocity correlations and high polar ordering; see Figs. 4(b) and 4(c). Increasing τ_R, while keeping $\tau_T/\tau_{\mathrm{MW}}$ below 2, leads to the emergence of stable rotating clusters (Video S3 in the Supplemental Material [29]), with (periodic) long-range spatial pair and velocity correlations. These structures likely arise from the complex interplay of hydrodynamic and electrostatic interactions between the Quincke walkers. While swarms are attributed to pair-aligning interactions [25,26,45], a recent model suggests that a competing antialigning interaction can lead to rotating clusters [46]. As the memory effect fades, $\tau_T/\tau_{\mathrm{MW}} > 2$, the stationary rotating clusters transition into mobile elongated clusters composed of a smaller number of particles. At small to intermediate values of τ_R, particles form stable large polar clusters (Video S4 in the Supplemental Material [29]) with long-range velocity and orientational order [shown in Figs. 4(a)–4(c)], which cruise over the whole domain without significant exchange of particles. Upon further increase of τ_T and τ_R, the giant polar clusters break up by exchanging outermost particles, which start performing independent random walks. This results in a more continuous spectrum of cluster size distribution at steady state, with large clusters being orientationally decorrelated; see Figs. 4(c) and 4(d). The resulting disordered clusters are highly dynamic: They continuously evolve, deform, and break by exchanging particles (Video S5 in the Supplemental Material [29]).

The cluster size distribution in Fig. 4(d) shows a kink at large particle size n, which can be fit by $P(n) \sim c_1 n^{b_1} e^{-n/n_{c1}} + c_2 n^{b_2} e^{-n/n_{c2}}$, whose scalings agree well with dynamic clustering in bacterial suspension and discrete particle simulations [47–49]. The particle number fluctuations ΔN scale with the average particle numbers $\langle N \rangle$ (in windows of different linear size) as $\Delta N \sim \langle N \rangle^a$, with exponent $a \sim 0.85$ (see Supplemental Material Fig. S7 [29]), larger than the one for fluctuations in thermal equilibrium $a = 0.5$. Furthermore, cluster mean velocity increases with the size of the cluster and plateaus beyond

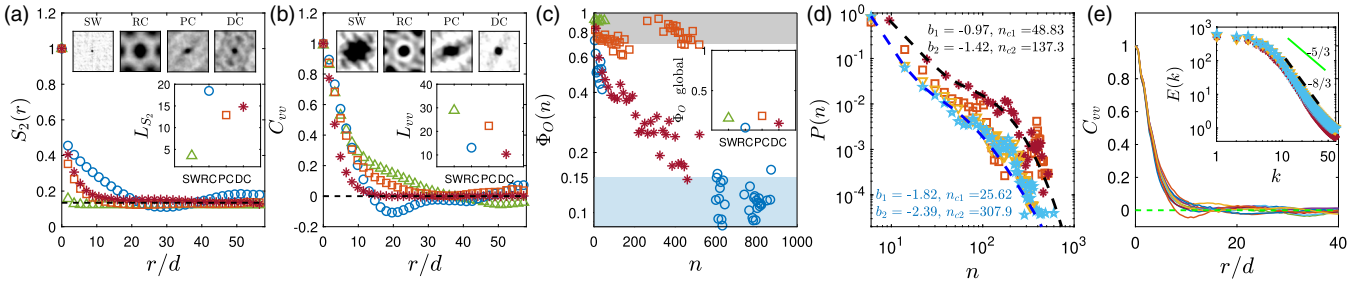

FIG. 4. (a) Angular-averaged normalized two-point correlation vs normalized radial distance r. Top inset: In 2D, showing the spatial periodicity of rotating cluster. Bottom inset: Characteristic length of S_2. Angular-averaged velocity autocorrelation vs normalized radial distance. Top inset: In 2D, showing the periodicity of velocity correlation of rotating and polar clusters in space. Some degree of anisotropy in the velocity autocorrelation of the polar cluster is due to insufficient number of clusters in the field of view. Bottom inset: Characteristic length of C_{vv}. (c) Polar order parameter vs n, the number of particles in a cluster. Inset: Global order parameter; shaded areas indicate polar ordering higher than 75% and lower than 15%. (d) Probability distribution of clusters with n number of particles. (e) VACF of a disordered cluster with $\tau_R = 100$ ms evaluated at different run steps. Inset: Angular-averaged energy spectrum of disordered clusters. Symbols denote different phases: □ polar cluster (PC) ($\tau_T/\tau_{\mathrm{MW}} = 3$, $\tau_R = 8$ ms), * disordered cluster (DC) ($\tau_T/\tau_{\mathrm{MW}} = 10$, $\tau_R = 40$ ms), ▽ disordered cluster ($\tau_T/\tau_{\mathrm{MW}} = 10$, $\tau_R = 100$ ms), ⋆ disordered cluster ($\tau_T/\tau_{\mathrm{MW}} = 10$, $\tau_R = 150$ ms), △ swarm (SW) ($\tau_T/\tau_{\mathrm{MW}} = 1$, $\tau_R = 4$ ms.

certain cluster sizes (see Supplemental Material Fig. S8 [29]), similar to Ref. [47]. The angular-averaged velocity autocorrelation of disordered clusters in Fig. 4(e) shows anticorrelation around $r/d \approx 10$–20, which is a signature for the formation of vortical structures similar to those observed in different bacterial systems [50–54]. The corresponding energy spectrum calculated from the velocity field of the particles shows scaling of $-8/3$ [see also Fig. 4(e)], which is in agreement with mesoscopic turbulence in bacterial suspension [53], discrete particle simulations [55], and also in numerical simulations for suspension of pushers in a Newtonian fluid [56]. The quantitative similarity of the cluster and flow statistics of bacterial and Quincke walker clusters may originate from a unique feature of the Quincke random walkers: When the field is on, they all run, and when the field is turned off, they all stop. This *de facto* synchronization of the runs and turns mimics the fact that in dense suspensions, bacteria do not swim independently due to mechanical locking of flagella [47,57].

In conclusion, the Quincke random walker provides a well-defined experimental system to study active fluids emulating bacterial suspensions. In this work, we only focused on the effects of the simple walk and its characteristics (run and turn times) on the collective dynamics at moderate particle density. Exploration of the complete phase space will likely uncover more complex collective states. While we only investigated the constant speed motility, the Quincke random walker can be easily programmed for runs with a general time-varying speed [58] and locomotions with distributed waiting times featuring anomalous subdiffusion. Our approach can also be used to randomize the motion of other active particles powered by the Quincke effect, such as the recently proposed helical propeller [59] and use this microswimmer to explore self-organization in three-dimensional suspensions. We envision the Quincke random walker as a new experimental platform to explore active locomotion at the microscale and a test bed for the abundant theoretical models of the collective dynamics of active matter.

This research has been supported by National Science Foundation Grants No. CBET-1704996, No. DMS-1716114, and No. CMMI-1740011.

[1] I. S. Aranson, Phys. Usp. **56**, 79 (2013).
[2] J. Zhang, E. Luijten, B. A. Grzybowski, and S. Granick, Chem. Soc. Rev. **46**, 5551 (2017).
[3] A. Zoettl and H. Stark, J. Phys. Condens. Matter **28**, 253001 (2016).
[4] J. Elgeti, R. G. Winkler, and G. Gompper, Rep. Prog. Phys. **78**, 056601 (2015).
[5] E. Lauga, Annu. Rev. Fluid Mech. **48**, 105 (2016).
[6] C. Dombrowski, L. Cisneros, S. Chatkaew, R. E. Goldstein, and J. O. Kessler, Phys. Rev. Lett. **93**, 098103 (2004).
[7] P. Illien, R. Golestanian, and A. Sen, Chem. Soc. Rev. **46**, 5508 (2017).
[8] S. J. Ebbens and D. A. Gregory, Acc. Chem. Res. **51**, 1931 (2018).
[9] K. Han, C. W. Shields IV, and O. D. Velev, Adv. Funct. Mater. **28**, 1705953 (2018).
[10] S. Palagi and P. Fischer, Nat. Rev. Mater. **3**, 113 (2018).
[11] H.-W. Huang, F. E. Uslu, P. Katsamba, E. Lauga, M. S. Sakar, and B. J. Nelson, Sci. Adv. **5**, eaau1532 (2019).
[12] W. F. Paxton, K. C. Kistler, C. C. Olmeda, A. Sen, S. K. St. Angelo, Y. Cao, T. E. Mallouk, P. E. Lammert, and V. H. Crespi, J. Am. Chem. Soc. **126**, 13424 (2004).
[13] J. R. Howse, R. A. L. Jones, A. J. Ryan, T. Gough, R. Vafabakhsh, and R. Golestanian, Phys. Rev. Lett. **99**, 048102 (2007).
[14] P. Tierno, R. Golestanian, I. Pagonabarraga, and F. Sagués, Phys. Rev. Lett. **101**, 218304 (2008).
[15] S. Gangwal, O. J. Cayre, M. Z. Bazant, and O. D. Velev, Phys. Rev. Lett. **100**, 058302 (2008).
[16] J. Palacci, S. Sacanna, A. P. Steinberg, D. J. Pine, and P. M. Chaikin, Science **339**, 936 (2013).
[17] H.-R. Jiang, N. Yoshinaga, and M. Sano, Phys. Rev. Lett. **105**, 268302 (2010).
[18] I. Buttinoni, G. Volpe, F. Kmmel, G. Volpe, and C. Bechinger, J. Phys. Condens. Matter **24**, 284129 (2012).
[19] L. Baraban, R. Streubel, D. Makarov, L. Han, D. Karnaushenko, O. G. Schmidt, and G. Cuniberti, ACS Nano **7**, 1360 (2013).
[20] J. R. Gomez-Solano, A. Blokhuis, and C. Bechinger, Phys. Rev. Lett. **116**, 138301 (2016).
[21] N. Narinder, C. Bechinger, and J. R. Gomez-Solano, Phys. Rev. Lett. **121**, 078003 (2018).
[22] S. Ebbens, R. A. L. Jones, A. J. Ryan, R. Golestanian, and J. R. Howse, Phys. Rev. E **82**, 015304(R) (2010).
[23] S. J. Ebbens, G. A. Buxton, A. Alexeev, A. Sadeghi, and J. R. Howse, Soft Matter **8**, 3077 (2012).
[24] J. R. G.-S. Celia Lozano and C. Bechinger, New J. Phys. **20**, 015008 (2018).
[25] A. Bricard, J.-B. Caussin, N. Desreumaux, O. Dauchot, and D. Bartolo, Nature (London) **503**, 95 (2013).
[26] A. Bricard, J.-B. Caussin, D. Das, C. Savoie, V. Chikkadi, K. Shitara, O. Chepizhko, F. Peruani, D. Saintillan, and D. Bartolo, Nat. Commun. **6**, 7470 (2015).
[27] G. E. Pradillo, H. Karani, and P. M. Vlahovska, Soft Matter **15**, 6564 (2019).
[28] G. Quincke, Ann. Phys. (Berlin) **295**, 417 (1896).
[29] See Supplemental Material at http://link.aps.org/supplemental/10.1103/PhysRevLett.123.208002 for videos, details of the experiments and analysis, and additional figures, which includes Refs. [30–38].
[30] J. R. Melcher and G. I. Taylor, Annu. Rev. Fluid Mech. **1**, 111 (1969).
[31] I. Turcu, J. Phys. A **20**, 3301 (1987).
[32] T. B. Jones, IEEE Trans. Ind. Appl. **20**, 845 (1984).
[33] W. Thielicke and E. J. Stamhuis, J. Open Res. Software **2**, e30 (2014).
[34] C. Bechinger, R. Di Leonardo, H. Löwen, C. Reichhardt, G. Volpe, and G. Volpe, Rev. Mod. Phys. **88**, 045006 (2016).
[35] F. Thiel, L. Schimansky-Geier, and I. M. Sokolov, Phys. Rev. E **86**, 021117 (2012).

[36] F. Detcheverry, Phys. Rev. E **96**, 012415 (2017).
[37] R. Bracewell, *The Fourier Transform and Its Applications* (McGraw-Hill, New York, 1965).
[38] S. Torquato, *Random Heterogeneous Materials: Microstructure and Macroscopic Properties* (Springer Science & Business Media, Berlin, 2013).
[39] A. Morin, D. Lopes Cardozo, V. Chikkadi, and D. Bartolo, Phys. Rev. E **96**, 042611 (2017).
[40] D. Geyer, A. Morin, and D. Bartolo, Nat. Mater. **17**, 789 (2018).
[41] E. Lemaire and L. Lobry, Physica (Amsterdam) **314A**, 663 (2002).
[42] H. C. Berg, *Random Walks in Biology* (Princeton University Press, Princeton, NJ, 1983).
[43] L. Angelani, Europhys. Lett. **102**, 20004 (2013).
[44] V. Zaburdaev, S. Denisov, and J. Klafter, Rev. Mod. Phys. **87**, 483 (2015).
[45] S. Q. Lu, b Bing Yue Zhang, Z. C. Zhang, Y. Shi, and T. H. Zhang, Soft Matter **14**, 5092 (2018).
[46] R. Großmann, P. Romanczuk, M. Bär, and L. Schimansky-Geier, Eur. Phys. J. Spec. Top. **224**, 1325 (2015).
[47] H. P. Zhang, A. Be'er, E.-L. Florin, and H. L. Swinney, Proc. Natl. Acad. Sci. U.S.A. **107**, 13626 (2010).
[48] O. Pohl and H. Stark, Phys. Rev. Lett. **112**, 238303 (2014).
[49] F. Peruani, J. Starruß, V. Jakovljevic, L. Søgaard-Andersen, A. Deutsch, and M. Bär, Phys. Rev. Lett. **108**, 098102 (2012).
[50] C. Dombrowski, L. Cisneros, S. Chatkaew, R. E. Goldstein, and J. O. Kessler, Phys. Rev. Lett. **93**, 098103 (2004).
[51] L. H. Cisneros, R. Cortez, C. Dombrowski, R. E. Goldstein, and J. O. Kessler, Exp. Fluids **43**, 737 (2007).
[52] H. P. Zhang, A. Be'er, R. S. Smith, E.-L. Florin, and H. L. Swinney, Europhys. Lett. **87**, 48011 (2009).
[53] H. H. Wensink, J. Dunkel, S. Heidenreich, K. Drescher, R. E. Goldstein, H. Löwen, and J. M. Yeomans, Proc. Natl. Acad. Sci. U.S.A. **109**, 14308 (2012).
[54] J. Dunkel, S. Heidenreich, K. Drescher, H. H. Wensink, M. Bär, and R. E. Goldstein, Phys. Rev. Lett. **110**, 228102 (2013).
[55] R. Großmann, P. Romanczuk, M. Bär, and L. Schimansky-Geier, Phys. Rev. Lett. **113**, 258104 (2014).
[56] G. Li and A. M. Ardekani, Phys. Rev. Lett. **117**, 118001 (2016).
[57] M. F. Copeland and D. B. Weibel, Soft Matter **5**, 1174 (2009).
[58] S. Babel, B. ten Hagen, and H. Löwen, J. Stat. Mech. (2014) P02011 (2014).
[59] D. Das and E. Lauga, Phys. Rev. Lett. **122**, 194503 (2019).